H_2 Double Ionization with Few-Cycle Laser Pulses

Sébastien Saugout, Eric Charron, Christian Cornaggia

H_2 double ionization with few–cycle laser pulses

S. Saugout

Laboratoire de Photophysique Moléculaire du CNRS

Université Paris-Sud, bâtiment 210, F–91405 Orsay, France and

Service des Photons, Atomes et Molécules

Direction des Sciences de la Matière, CEA Saclay,

bâtiment 522, F–91191 Gif-sur-Yvette, France

E. Charron

Laboratoire de Photophysique Moléculaire du CNRS

Université Paris-Sud, bâtiment 210, F–91405 Orsay, France

C. Cornaggia

Service des Photons, Atomes et Molécules

Direction des Sciences de la Matière, CEA Saclay,

bâtiment 522, F–91191 Gif-sur-Yvette, France

Abstract

The temporal dynamics of double ionization of H_2 has been investigated both experimentally and theoretically with few–cycle laser pulses. The main observables are the proton spectra associated to the $H^+ + H^+$ fragmentation channel. The model is based on the time–dependent Schrödinger equation and treats on the same level the electronic and nuclear coordinates. Therefore it allows to follow the ultrafast nuclear dynamics as a function of the laser pulse duration, carrier–envelope phase offset and peak intensity. We mainly report results in the sequential double ionization regime above 2×10^{14} Wcm^{-2}. The proton spectra are shifted to higher energies as the pulse duration is reduced from 40 fs down to 10 fs. The good agreement between the model predictions and the experimental data at 10 fs permits a theoretical study with pulse durations down to a few femtoseconds. We demonstrate the very fast nuclear dynamics of the H_2^+ ion for a pulse duration as short as 1 fs between the two ionization events giving respectively H_2^+ from H_2 and $H^+ + H^+$ from H_2^+. Carrier–envelope phase offset only plays a significant role for pulse durations shorter than 4 fs. At 10 fs, the laser intensity dependence of the proton spectra is fairly well reproduced by the model.

PACS numbers: 33.80.Rv, 33.80.Eh, 42.50.Vk

I. INTRODUCTION

Recent outstanding advances in ultrafast laser physics have led to the generation of few–cycle pulses in the near–infrared and visible ranges [1, 2] and in the XUV range [3, 4]. Very efficient spectral techniques are used for a complete reconstruction of the electric field in the temporal domain. In the infrared and visible ranges, these techniques are known as frequency–resolved optical gating (FROG) [5] and spectral phase interferometry for direct electric field reconstruction (SPIDER) [6]. In the XUV range, the conventional optical elements used for FROG and SPIDER cannot be used. In consequence, the attosecond pulse is reconstructed from spectral informations based on the photoionization of atoms in the gas phase. In the first attosecond experiments, the spectral phase was measured through two–photon, two–color photoionization of atoms [3, 4]. More recently, an extension of the FROG concept to the XUV photoionization was proposed and successfully applied to the measurement of attosecond pulses [7, 8].

Following these developments, this report deals with the temporal dynamics of double ionization of the H_2 molecule induced by near–infrared few–cycle intense laser pulses in the 10^{14}–10^{15} Wcm^{-2} intensity range. The strong field response of the H_2 molecule and its related molecular ion and isotopic species have been extensively studied in the past [9, 10, 11]. However, the H_2–laser interaction remains a subject of great interest for few–cycle laser pulses because of the attosecond electronic and femtosecond nuclear time scales and the relatively simple decay channels (ionization and dissociation) leading to H_2^+, $H^+ + H$, and $H^+ + H^+$. For instance in D_2, the $D^+ + D$ channel was used to propose the idea of an attosecond molecular clock based on the rescattering dynamics of the first ionized electron leading to the dissociation of the D_2^+ ion [12]. The same excitation scheme and dissociation channel were recently studied in order to control the electron localization with 5–fs carrier–envelope–phase–locked laser pulses [13]. We have recently shown that the proton spectrum allows to detect the presence of a pre–pulse or a post–pulse using a 10–fs pump–probe scheme [14] and the important concept of charge resonance enhanced ionization introduced by Bandrauk *et al.* [15].

In H_2, double ionization leads to two bare protons. In consequence, our main experimental and theoretical diagnostic is the proton spectrum as a function of the pulse duration, carrier–envelope offset phase, and intensity. Double ionization induced by few–cycle laser pulses

exhibit two regimes : nonsequential double ionization at low laser intensities below 2×10^{14} Wcm^{-2} and sequential ionization at higher laser intensities [16, 17, 18, 19, 20, 21]. Charge resonance enhanced ionization belongs to the sequential ionization regime. However, it does not occur for few–cycle laser pulses because of the ultrashort pulse duration. After the first ionization event of H_2, the resulting H_2^+ molecular ion does not have enough time to stretch and to reach the internuclear distance range where enhanced ionization takes place [15]. Nonsequential double ionization has been studied in detail with an emphasis on the rescattering dynamics [17, 19]. Here we propose an experimental and theoretical study of the sequential regime at intensities above 2×10^{14} Wcm^{-2} where rescattering is less important [18]. The interesting feature is the time delay between the first and second electron removals. For few–cycle laser pulses this time delay might be expected to be a few femtoseconds corresponding to the pulse risetime. In the meantime, a nuclear wave packet arises in the H_2^+ molecular ion from the nonresonant coupling of the ground electronic state $X^2\Sigma_g^+$ and the first excited dissociative state $A^2\Sigma_u^+$. Therefore the delayed ejection of the second electron takes place during the evolution of the molecular ion internuclear distance. The resulting proton spectrum is shifted to lower energies in comparison to what might be expected from an instantaneous two–electron ejection.

In spite of the simplicity of the above picture , a quantitative prediction of the proton spectrum as a function of the ultrashort pulse parameters is not straightforward because of the complicated nonlinear couplings leading to single and double ionizations. In addition, the evolution of the nuclear wave packet of the intermediate H_2^+ ion has to be included in the theoretical framework. Usually this problem is solved using a two–step approach [16, 18]. After the first ionization event, the nuclear evolution of the H_2^+ ion is solved by numerical integration of the time–dependent Schrödinger equation. The initial wave packet is given by the projection of the H_2 ground vibrational state onto the different ion vibrational states. The second ionization event leading to double ionization is then calculated as a function of the time–dependent vibrational wave packet. Tong and Lin give a clear account of the procedure in Ref. [18]. Here we propose a complementary approach for the quantitative analysis of our experimental results. Double ionization is treated using a unified approach based on a two–electron model where the internuclear distance remains a full quantum variable in order to extract the nuclear dynamics during the interaction. This model has been used in a recent paper [22] for the study of the mechanisms leading to double ionization

with 1–fs laser pulses. This manuscript focuses on other effects and on a more detailed comparison with experiments.

The paper is organized as follows. The experimental set–up is presented in Section II including the 10–fs pulses generation set–up and the time–of–flight detection of the ions. The theoretical model is described in Section III with an emphasis on a realistic field–free molecular description. In Section IV, the experimental results are compared to the theoretical predictions for a better understanding of the ionization and fragmentation mechanisms. In Section IV, pulse duration, carrier–envelope phase, and intensity dependences of the proton spectra are successively presented and discussed. Since the carrier–envelope phase of our 10–fs pulses is not controlled experimentally, this dependence will be commented from theoretical predictions only. The conclusions are finally summarized in the last section.

II. EXPERIMENTAL SET–UP

A. Laser system and pulse compression method

The ultrashort pulse generation set–up is based on a 1–kHz titanium:sapphire laser system and a hollow fibre pulse compression stage. The 1–kHz laser chain is built following the conventional chirp–pulse–amplification scheme [23]. It consists of an oscillator, a stretcher, a regenerative amplifier, and a compressor. The system delivers pulses with energies up to 600 μJ, duration of 40 fs, and a central wavelength of 795 nm. The pulse compression stage is designed following techniques introduced by Nisoli *et al.* [1] and Sartania *et al.* [2]. The laser beam is focused with a 700–mm–focal–length lens onto the tip of a 700–mm–long hollow fibre with a 250–μm inner diameter. The hollow fibre is housed on a V–groove in a chamber filled with argon gas. The non–linear Kerr effect in argon leads to self–phase modulation and wavelength spectrum broadening while the fibre waveguide ensures a spatially–homogeneous spectral broadening. Optimum argon operating pressures were found around 700 mbar for 40–fs and 600–μJ input laser pulses.

Figure 1 shows the wavelength spectra before and after the hollow fibre filled with argon. Self–phase modulation leads to a noticeable broadening. The usual multi–peak structure is observed as in other studies [1, 2]. The oscillatory behavior comes from interferences of waves with the same frequency but generated at different times within the laser pulse. The overall

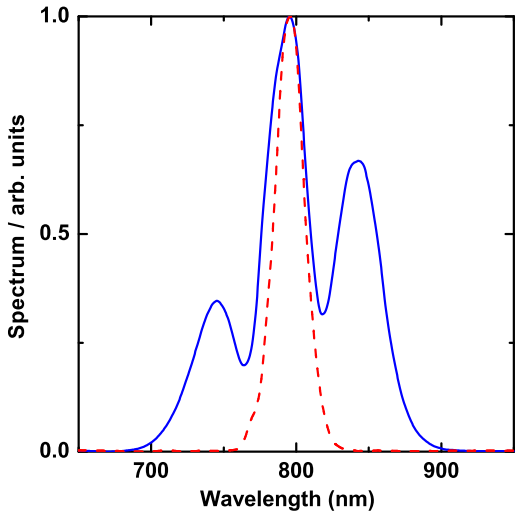

FIG. 1: (Color online) Wavelength spectra before (dashed curve) and after the hollow fibre (full curve) filled with argon gas. The argon pressure is 700 mbar. The laser pulse energy and duration are respectively 600 μJ and 40 fs.

transmission of the hollow fibre set–up including all the optical elements is above 50 %. After recollimation by an $f = 1$ m concave silver mirror, pulses are recompressed to 10 fs using several reflections on commercial broadband chirped mirrors. The pulse duration is measured using a home–made interferometric autocorrelator. Figure 2 presents an interferometric autocorrelation of 10–fs pulses corresponding to the wavelength spectrum presented in Fig. 1. The measured autocorrelation signal is compared to a calculated interferometric autocorrelation assuming a constant spectral phase. The good agreement between the measured and calculated curves shows that the chirped–mirrors compression stage works well for the second–order group delay dispersion compensation. The remaining disagreement comes from cubic and quartic residual phase that cannot be compensated with our set–up. The laser pulse duration relative uncertainty is estimated to be ± 20 %. Ultrashort 10–fs pulses with energies above 200 μJ are therefore available for subsequent experiments.

The pulse duration measurement presented in Fig. 2 has been recorded after the optimization of the group delay dispersion. This optimization is only valid for the autocorrelator because the chirped mirrors compressor is tuned in order to compensate for the air travel

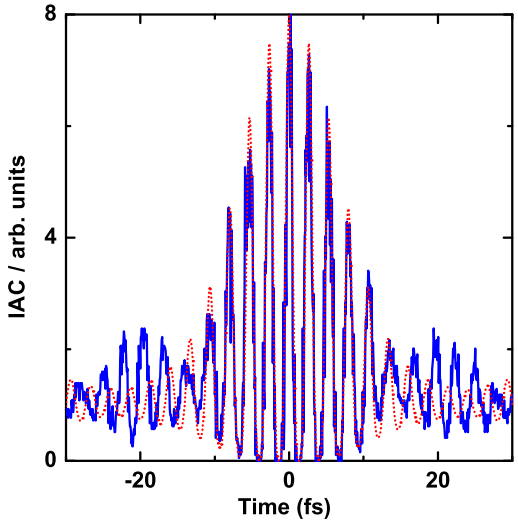

FIG. 2: (Color online) Interferometric autocorrelation (IAC) of 10–fs laser pulses. The experimental and calculated signals are given respectively by the full and dotted curves. The IAC curve is calculated using the Fourier transform of the frequency domain electric field, assuming a constant spectral phase.

to the autocorrelator and also for the small amount of group delay dispersion introduced by this device. The proton spectra are recorded in a vacuum chamber which is located elsewhere in the laboratory and which introduces a different group delay dispersion than the autocorrelator. Therefore the pulse duration will have to be optimized *in situ* at the location where the laser–molecule interaction takes place. The method is to introduce more negative group delay dispersion than necessary and then to compensate for it with a variable thickness of fused silica which exhibits a positive dispersion of 36.1 $fs^2 rad^{-1} mm^{-1}$. Proton spectra are systematically recorded for different fused silica thicknesses. As expected, the overall proton spectrum is shifted to the highest energy for the shortest pulse duration. This optimization procedure will be commented in more detail in Section IV since it involves a thorough understanding of the molecular response.

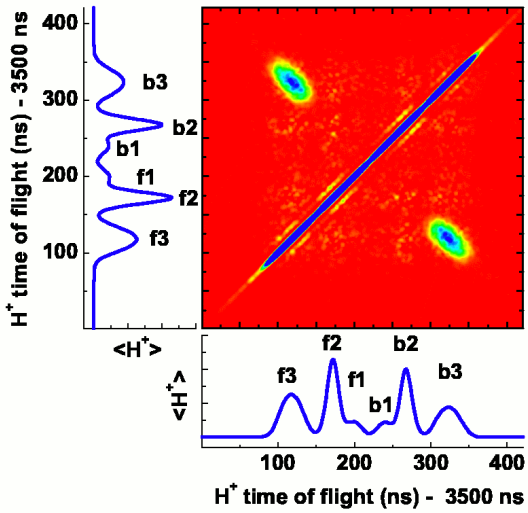

FIG. 3: (Color online) Covariance map from H_2 recorded with linearly–polarized 40–fs laser pulse at $I = 2 \times 10^{14}$ Wcm^{-2} and $p(H_2) = 5 \times 10^{-8}$ mbar. The collection electric field is 25 Vcm^{-1}. The bottom and left panels represent the usual proton time–of–flight spectrum and the central panel represents the covariance map. The f1, f2, and f3 peak labels correspond to protons ejected towards the detector. The b1, b2, and b3 labels are associated to protons ejected backwards the detector.

B. Ion detection set–up

The ultrashort pulses are sent in an ultrahigh vacuum chamber equipped with a 75–mm–focal–length on–axis parabolic mirror which allows to get laser intensities up to 10^{16} Wcm^{-2}. The hydrogen gas is introduced through an effusive gas jet at very low pressures down to 3×10^{-10} mbar which is the residual pressure of the chamber. Molecular hydrogen ions and protons are detected using a 1150–mm–long time–of–flight spectrometer based on the Wiley–McLaren configuration and devoted to experimental studies of multiple ionization [24, 25]. Fragmentation channels and the associated kinetic energy release spectra are determined using covariance mapping introduced by Frasinski *et al.* [26, 27]. In particular for H_2, it is important to separate the $H^+ + H^+$ double ionization channel from the $H^+ + H$ single ionization channel.

We recall here the main features of this technique. First of all, it allows to work with more than one ionization event per laser shot. Fragments coming from the same dissociation channel are expected to produce time–of–flight signals that fluctuate following a same pattern on a shot–to–shot basis. For fragmentation channels involving two detected bodies, the covariance coefficient $C_2(T_1, T_2)$ therefore measures the statistical correlation of fragments arriving at times T_1 and T_2. The method is illustrated in Fig. 3. The conventional time–of–flight proton spectrum is represented in the bottom panel. The time–of–flight signal has been delayed by 3500 ns in order to record only the significant proton signals. The proton spectrum is highly symmetric around the relative time of flight 220 ns and exhibits 3 peaks of protons emitted towards the detector and labeled f1, f2, and f3. The peaks labeled b1, b2, and b3 are associated to protons emitted backwards the detector. Let us recall here that the proton time of flight T is given by $T = T_0 \pm P/eF_c$, where T_0 is the time of flight of a proton with a zero initial momentum, P is the modulus of the initial momentum, the $\pm$ sign is positive for a proton emitted away from the detector and negative for a proton emitted towards the detector, F_c is the collection electric field ($F_c = 25$ Vcm^{-1} in these experiments) and e is the elementary charge [27]. In addition our spectrometer exhibits a strong angular discrimination due to its large longitudinal dimension. Therefore it allows the detection of protons with an initial momentum parallel to its axis. Since the angular discrimination is stronger for backwards protons, the backwards peaks b1, b2, and b3 in Fig. 3 are slightly smaller than the f1, f2, and f3 peaks associated to forwards protons.

The covariance coefficient $C_2(T_1, T_2)$ is represented in the central map in Fig. 3. For an easy visualization of the correlations, the conventional proton time–of–flight spectrum is also represented in the vertical left panel. A correlation between peaks f3 and b3 clearly appears in Fig. 3 and corresponds to the Coulomb explosion channel $H^+ + H^+$. The peaks f1 and f2 and their associated backwards peaks b1 and b2 are not correlated with any other peaks. They are associated to the $H^+ + H$ dissociation channel. Following the relationship between the time of flight and the momentum, the proton kinetic energy release spectra are extracted from the time–of–flight data using the associated time–to–energy normalization factors. Some proton energy spectra are represented in Fig. 4. The bottom curves represent the total and the $H^+ + H^+$ covariance energy spectra extracted from the time–of–flight data presented in Fig. 3. Although there remains some covariance noise for protons coming from $H^+ + H$, the proton spectrum associated to the $H^+ + H^+$ channel is unambiguously identified

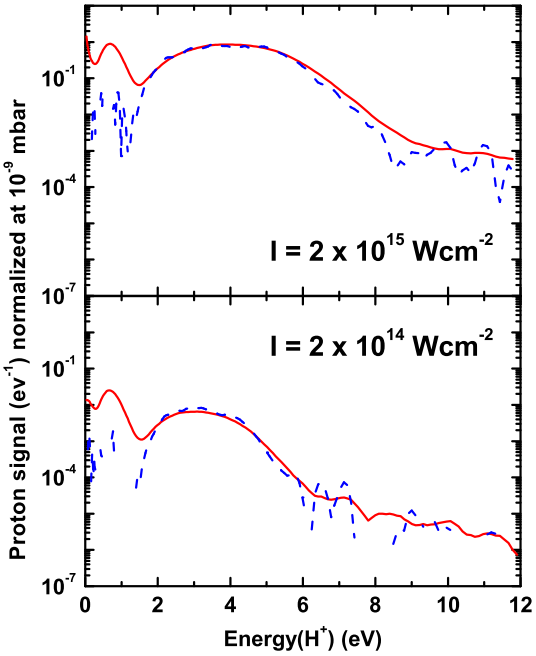

FIG. 4: (Color online) Proton spectra from H_2 recorded with linearly–polarized 40–fs laser pulse at $I = 2 \times 10^{14}$ Wcm^{-2} and $I = 2 \times 10^{15}$ Wcm^{-2}. For each laser intensity, the full curve represents the total proton spectrum and the dashed curve represents the covariance proton spectrum from the $H^+ + H^+$ dissociation channel.

as the broad peak above 1.5 eV of the conventional proton energy spectrum. Therefore in the following, we only present conventional proton spectra which exhibit a better statistics than the covariance spectra.

III. THEORETICAL TREATMENT

This section introduces the theoretical background and numerical methods we have developed for studying strong field Coulomb explosion dynamics of the hydrogen molecule.

A. The molecular system and the laser–molecule interaction

We follow the double ionization dynamics of the H_2 molecule by solving the time–dependent Schrödinger equation for the electronic and nuclear motions

$$i\hbar \frac{\partial}{\partial t}\chi_s \Psi(\boldsymbol{R}, \boldsymbol{r}, t) = \left[\hat{\mathcal{H}}_0 + V_{\rm int}\right] \chi_s \Psi(\boldsymbol{R}, \boldsymbol{r}, t)\,, \tag{1}$$

where $\hat{\mathcal{H}}_0$ is the field–free Hamiltonian and $V_{\rm int}$ the field–molecule interaction potential. The body-fixed coordinate $\boldsymbol{r} \equiv \{\boldsymbol{r}_1, \boldsymbol{r}_2\}$ refers here to the electrons, while $\boldsymbol{R}$ represents the internuclear vector. The electronuclear wave packet is denoted by $\chi_s \Psi(\boldsymbol{R}, \boldsymbol{r}, t)$, where χ_s is an antisymmetric two–electron spin wave function, while the spatial wave function $\Psi(\boldsymbol{R}, \boldsymbol{r}, t)$ is symmetric with respect to the exchange of the two electrons (singlet state). This approach does not assume a separation of the electronic and nuclear coordinates, thus going beyond the usual Born-Oppenheimer approximation.

The Hamiltonian of the field–free diatomic molecule is expressed as

$$\hat{\mathcal{H}}_0 = \hat{T}_n + \frac{1}{R} + V_{12}\left(\boldsymbol{r}_1 - \boldsymbol{r}_2\right) + \sum_{i=1,2} \hat{h}_i\,, \tag{2}$$

where $\hat{T}_n$ is the nuclear kinetic operator and $V_{12}(\boldsymbol{r}_1 - \boldsymbol{r}_2)$ the inter–electronic repulsion. The mono–electronic Hamiltonians $\hat{h}_i$ are expressed as the sum of the electronic kinetic operator and the electron–nuclei interaction potential

$$\hat{h}_i = -\frac{\hbar^2}{2m}\nabla_i^2 + V_{en}(\boldsymbol{R}, \boldsymbol{r}_i)\,. \tag{3}$$

The ionization dynamics is initiated by the length gauge radiative coupling

$$V_{\rm int}(\boldsymbol{r}_1, \boldsymbol{r}_2, t) = -e\left(\boldsymbol{r}_1 + \boldsymbol{r}_2\right) \cdot \boldsymbol{E}(t) \tag{4}$$

associated, in the dipole approximation, with the linearly polarized classical electric field

$$\boldsymbol{E}(t) = E_0\, f(t) \cos(\omega t + \varphi)\, \hat{\boldsymbol{e}}\,, \tag{5}$$

where E_0 is the field amplitude, ω the angular frequency, and φ the carrier–envelope offset phase. The pulse shape is given by the Gaussian–like expression

$$f(t) = \sin^2\left(\frac{\pi t}{\tau}\right)\,, \tag{6}$$

with total pulse duration τ. The frequency ω corresponds to a central wavelength of 800 nm and the internuclear coordinate $\boldsymbol{R}$ is constrained along the field polarization vector $\hat{\boldsymbol{e}}$. The two electrons, of coordinates $\boldsymbol{r}_i = z_i\,\hat{\boldsymbol{e}}$, are also assumed to oscillate along this axis. Recent numerical studies have indeed shown that two-electron dynamics in molecules is mainly characterized by a one-dimensional motion in linear polarization [28, 29].

In order to mimic the dynamics of the real H_2 molecule, we have introduced two R–dependent softening parameters $\alpha(R)$ and $\beta(R)$ in the Coulomb potentials describing the electron–electron

$$V_{12}(z_1 - z_2) = \left[(z_1 - z_2)^2 + \alpha^2(R)\right]^{-\frac{1}{2}} \tag{7}$$

and electron-nuclei interactions

$$V_{en}(R, z_i) = -\sum_{s=\pm 1} \left[(z_i + s \times R/2)^2 + \beta^2(R)\right]^{-\frac{1}{2}} . \tag{8}$$

These two softening parameters are assumed to vary slowly with the internuclear distance. In a first step, the parameter $\beta(R)$ is adjusted at each internuclear distance in order to reproduce the energy of the ground electronic state of H_2^+ [30]. The parameter $\alpha(R)$ is then obtained by reproducing the energy of the ground electronic state of the hydrogen molecule [31]. These potential curves, presented in Fig. 5, confirm that the adjustment of these two parameters allows for an accurate reproduction of the exact molecular potentials even though the electronic problem is presently reduced to a single dimension. The variation of these two parameters with the internuclear distance is given in Fig. 6.

B. The electronuclear wave packet propagation and the initial H_2 wavefunction

In order to calculate the single and double ionization of the hydrogen molecule submitted to an intense and pulsed laser radiation, we propagate the total wave function $\Psi(\boldsymbol{R}, \boldsymbol{r}, t)$ in time during the entire pulse using the split operator method developed by Feit et al. [32]

$$\Psi(\boldsymbol{R}, \boldsymbol{r}, t + \delta t) = \mathrm{e}^{-i\left[\hat{\mathcal{H}}_0 + V_{\mathrm{int}}\right]\delta t/\hbar}\ \Psi(\boldsymbol{R}, \boldsymbol{r}, t)\,, \tag{9}$$

where the total Hamiltonian $\hat{\mathcal{H}}_0 + V_{\mathrm{int}} = \hat{T} + \hat{V}(t)$ is split in two parts corresponding to the kinetic and potential propagations

$$\begin{aligned} \mathrm{e}^{-i\left[\hat{\mathcal{H}}_0 + V_{\mathrm{int}}\right]\delta t/\hbar} \;=\; & \mathrm{e}^{-i\,\hat{T}\,\delta t/2\hbar}\ \mathrm{e}^{-i\,\hat{V}(t)\,\delta t/\hbar} \\ & \times \mathrm{e}^{-i\,\hat{T}\,\delta t/2\hbar} + o(\delta t^3)\,. \end{aligned} \tag{10}$$

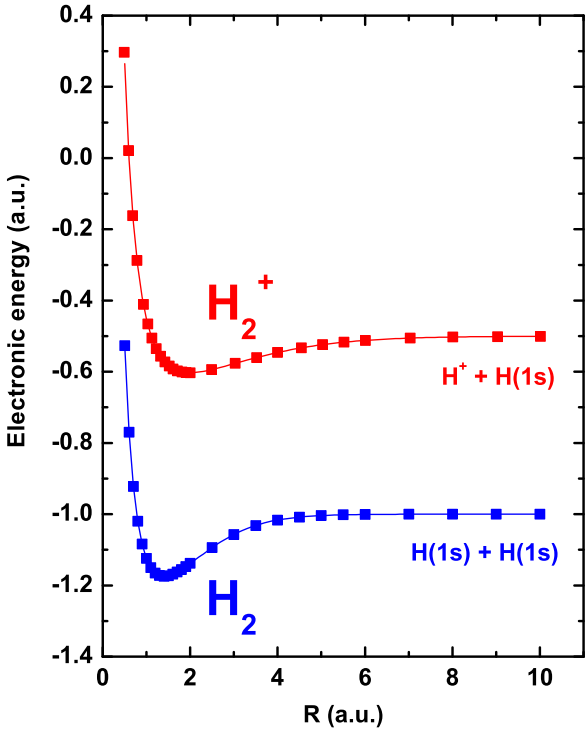

FIG. 5: (Color online) Calculated potential curves of the electronic ground states of H_2 and H_2^+. Squares are obtained from the model presented in the paper and full curves are the *ab initio* energies reported in Refs. [30, 31].

$\hat{T}$ represents here the sum of the nuclear and electronic kinetic energy operators, while $\hat{V}(t)$ includes all potential operators. The kinetic and potential propagations are performed in the momentum and coordinate spaces respectively. Three-dimensional Fast Fourier Transformation (FFT) allows rapid passage back and forth from one representation to the other at each time step. Typical grids extend up to $z_1^{\max} = z_2^{\max} = 100\,a_0$ and $R^{\max} = 10\,a_0$ with $(512)^3$ grid points. A time step of $\delta t \simeq 1$ as is necessary to achieve convergence. For very short pulse durations, an additional field free propagation is performed after the end of the pulse in order to give enough time for the ionized electrons to reach the asymptotic region were the wave function can be analyzed (see Sec. III C hereafter).

The initial wave function $\Psi(\boldsymbol{R}, \boldsymbol{r}, t = 0)$ is taken as the ground nuclear and electronic state of the hydrogen molecule, calculated within the present non–Born–Oppenheimer model using the imaginary time relaxation technique [33]. The equilibrium internuclear distance of

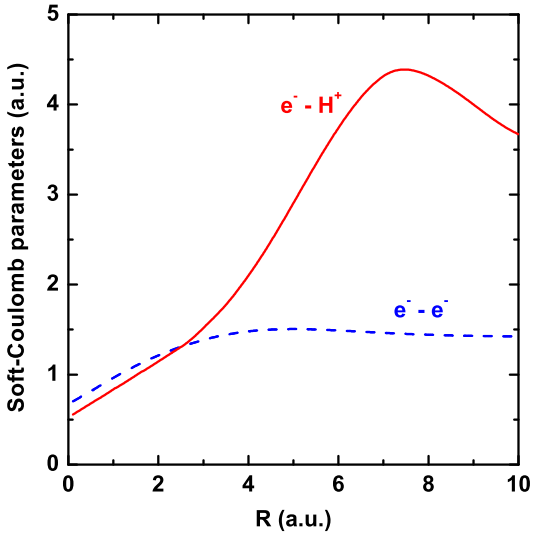

FIG. 6: (Color online) Soft–Coulomb parameters. The full curve and the dashed curves represent respectively the electron–nuclei and the electron–electron smoothing parameters.

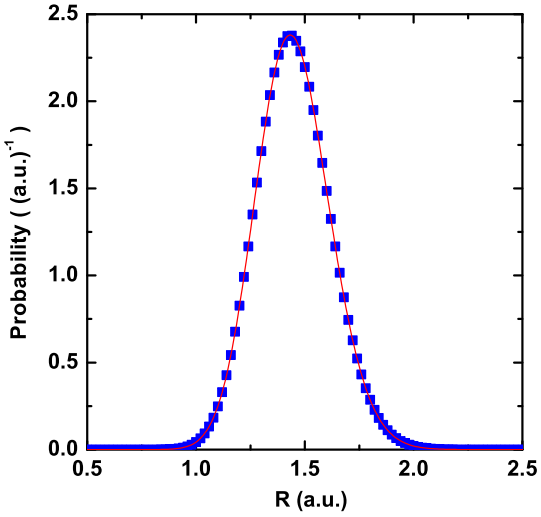

FIG. 7: (Color online) Probability density from the vibrational ground state of H_2. Full curve: This model. Squares: Calculated from the *ab initio* ground electronic state $v = 0$ of H_2 given in Ref. [31].

H_2 , $R_e \simeq 1.4\, a_0$, is perfectly reproduced, and Fig. 7 shows the very good agreement obtained between the nuclear probability density

$$P(R) = \iint |\Psi(\boldsymbol{R}, \boldsymbol{r}, t = 0)|^2 \; dz_1 \, dz_2 \,, \tag{11}$$

calculated here and the probability density $\chi_v^2(R)$ of the ground vibrational state $v = 0$ of H_2 calculated from the Born–Oppenheimer ground electronic state potential given in Ref. [31].

C. The wave packet analysis

The single and double ionization probabilities are analyzed using a well–established cartography technique [34]. The plane (z_1, z_2) is partitioned in three regions Γ_0, Γ_1 and Γ_2 corresponding respectively to H_2, H_2^+, and H_2^{2+}. Double ionization occurs in the asymptotic region $\Gamma_2 \equiv \{|z_1|, |z_2| > z_A\}$ with $z_A = 20\, a_0 \gg R_e$. The single ionization region Γ_1 is defined as $\{|z_i| < z_A,\ |z_j| > z_A\}$, and the neutral H_2 molecule is found in the region $\Gamma_0 \equiv \{|z_1|, |z_2| \leqslant z_A\}$. A schematic illustration of these three regions is given in Fig. 8 which represents the partition of the (z_1, z_2) plane. The outgoing ionization flux is accumulated during the time propagation in the regions Γ_1 and Γ_2 to extract the single and double ionization probabilities as a function of time. Absorbing boundaries are imposed at the end of the grid to avoid spurious reflection effects.

To extract the proton kinetic energy distributions $S(E, t)$ obtained after Coulomb explosion, we use a simple mapping which relates $S(E, t)$ to the probability density

$$P_2(R, t) = \iint_{\Gamma_2} |\Psi(\boldsymbol{R}, \boldsymbol{r}, t)|^2 \; dz_1 \, dz_2 \,, \tag{12}$$

in the Γ_2 region, using the Coulomb relation $E = 0.5/R$ and the requirement of particle conservation

$$P_2(R, t)\, dR = S(E, t)\, dE \,. \tag{13}$$

The kinetic energy E denotes here the energy of a single proton. The energy distribution $S(E, t)$ is finally accumulated over the entire time propagation to obtain the kinetic energy release spectrum $S(E)$ which is measured in experiments.

Figure 9 represents the comparison between an experimental proton spectrum recorded at 4×10^{14} Wcm^{-2} with a pulse duration of 10 fs and two spectra calculated at the same laser

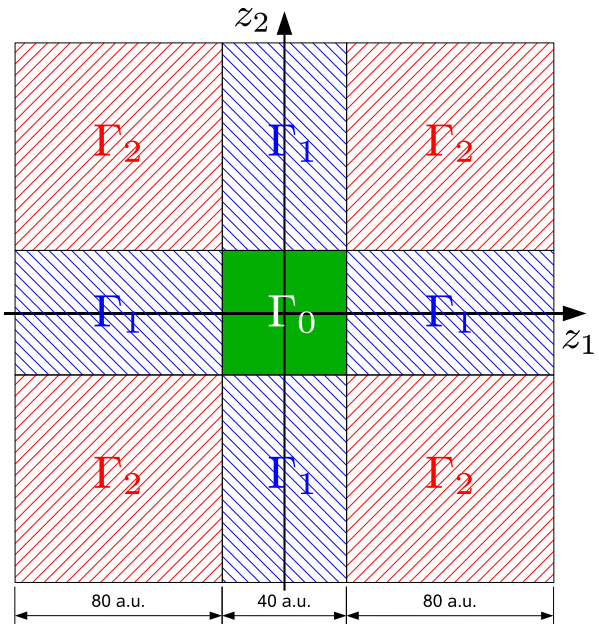

FIG. 8: (Color online) Partition zones of the electrons coordinates z_1 and z_2. The three regions Γ_0, Γ_1 and Γ_2 correspond respectively to the H_2, $H_2^+ + e^-$, and $H_2^{2+} + e^- + e^-$ systems.

intensity with pulse durations of respectively 10 fs and 12 fs. The proton peak associated to the $H^+ + H^+$ channel is better reproduced with a 12–fs pulse duration than with a 10–fs duration. It is quite noticeable that a relatively small variation of 2 fs leads to a measurable proton energy shift. Concerning the agreement with the experimental data, the very high sensitivity of the proton spectra might explain the discrepancy between the experimental and theoretical proton spectra at 10 fs when one takes into account the relative accuracy of the pulse duration and laser intensity measurements. In the following, we choose to compare the experimental data with calculations performed with a pulse duration of 10 fs in order to deal with a theoretical model without any adjustable parameter. The agreement at different laser intensities will be commented more thoroughly in Section IV.

IV. RESULTS AND DISCUSSION

A. Pulse duration dependence of proton spectra

This section is devoted to the dependence of the proton spectra as a function of the pulse duration. The comparisons between different pulse durations are performed while keeping

the same peak laser intensity. For instance, Fig. 10 represents two proton spectra recorded at 8×10^{14} Wcm^{-2} with respectively 40–fs and 10–fs laser pulses. Both spectra exhibit the above–mentioned separation between the $H^+ + H$ and $H^+ + H^+$ dissociation channels. In particular for this last channel, the proton spectra have maxima at 3.8 eV at 40 fs and 5.5 eV at 10 fs. We first would like to emphasize the large shift of 1.7 eV when the pulse duration is reduced from 40 fs to 10 fs. It is also important to notice that double ionization cannot be considered as an instantaneous double ionization process at 10 fs since such a sudden electrons removal would produce a proton spectrum peaked at 9.2 eV. This instantaneous two–electron emission would lead to the proton spectrum represented in Fig. 11 by the far right curve. The corresponding calculation is based on the projection of the population of the $v = 0$ vibrational state of H_2 represented in Fig. 7 onto the $H^+ + H^+$ repulsion curve with the appropriate normalization factors. The interpretation is here straightforward: After the first ionization step, enough time is left to the H_2^+ ion for a significant stretching before the second ionization event. The proton peak shifts towards higher energies at 10 fs since the internuclear distance is reduced because of the shorter pulse duration.

To the best of our knowledge, intense infrared laser pulses with durations below a few femtoseconds are not yet available. Theoretical predictions thus become highly desirable

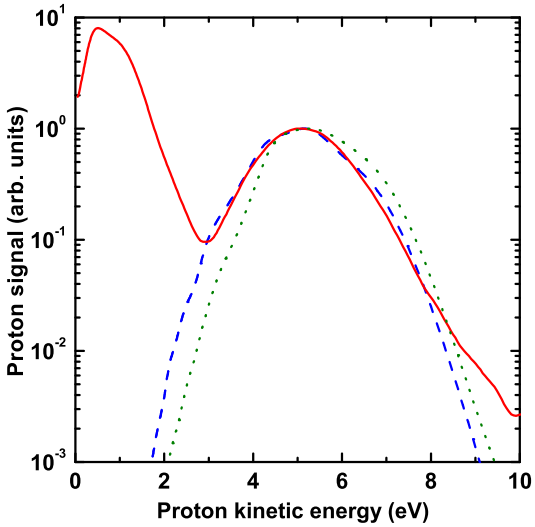

FIG. 9: (Color online) Proton spectra from H_2 at 4×10^{14} Wcm^{-2}. Full curve: Experimental with a pulse duration of 10 fs. Dotted curve: Theoretical with a pulse duration of 10 fs. Dashed curve: Theoretical with a pulse duration of 12 fs.

in order to know the H_2 molecule sensitivity to ultrashort pulses. Figure 11 shows five calculated proton spectra from right to left which correspond to the instantaneous two–electron ionization for the far right spectrum and then to pulse durations of respectively 1 fs, 2 fs, 4 fs, and 10 fs. The laser peak intensity remains 8×10^{14} Wcm^{-2} as in the experimental results in Fig. 10. All curves have been normalized to unity for an easier comparison. The calculations are performed with a zero carrier–envelope offset phase. The most striking feature comes from the proton spectrum calculated with a 1–fs pulse duration. The spectrum peaks at 8 eV and is therefore already shifted by 1.2 eV towards lower energies in comparison with the proton spectrum from instantaneous double ionization. Even for such an ultrashort laser pulse, nuclear motion takes place and leads to a measurable shift of the proton spectrum. As for the experimental spectra presented in Fig. 10, the theoretical proton spectra are shifted to lower energies as the pulse duration is increased from 1 fs to 10 fs. The spectrum calculated et 10 fs peaks around 5.3 eV, again in good agreement with the measurement shown in Fig. 10.

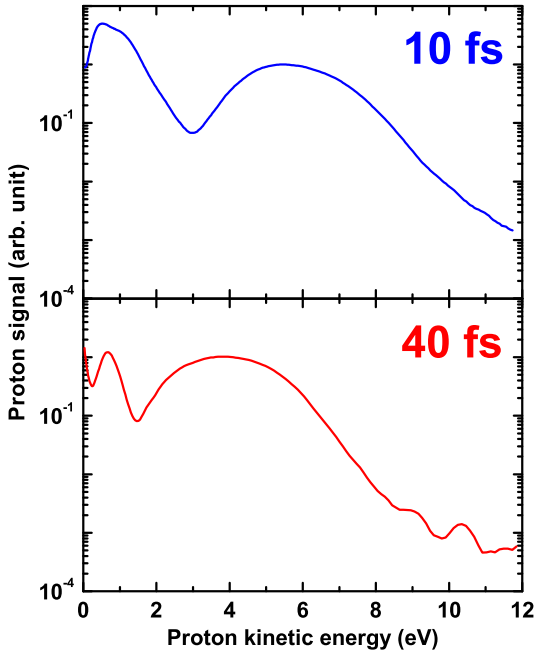

FIG. 10: (Color online) Proton spectra from H_2 at 8×10^{14} Wcm^{-2} recorded with pulse durations of 40 fs and 10 fs.

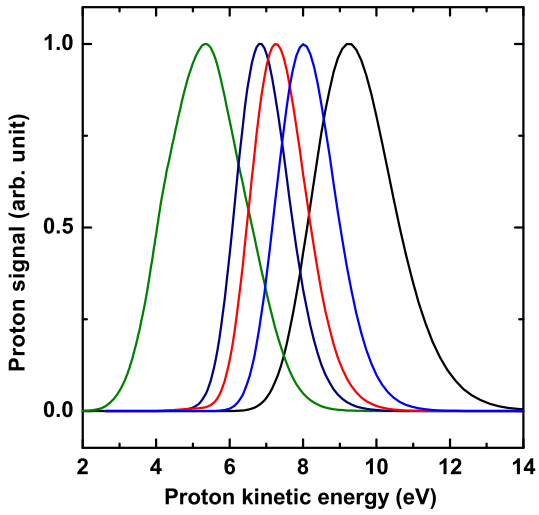

FIG. 11: (Color online) Proton spectra from H_2 calculated at 8×10^{14} Wcm^{-2} for different pulse durations. From right to left: "0", 1, 2, 4, and 10 fs. The "0"–fs pulse duration spectrum represents what is expected from an instantaneous two–electron ionization of H_2.

The above experimental and theoretical results give an *a posteriori* justification of our experimental method of the pulse optimization. Indeed, the optimization of the ultrashort pulse duration can be performed *in situ* inside the ion spectrometer using the proton spectrum since it shifts to higher energies as the pulse duration is decreased. After the initial pulse duration optimization using the interferometric autocorrelator, the proton spectra are recorded with different thicknesses of fused silica inserted in the beam just before the ion spectrometer entrance window. An optimum of the proton spectrum to higher energies is systematically looked for. If such an optimum is not found, then additional negative group delay dispersion is introduced in the compressor by adding additional bounces onto the chirped mirrors. Figure 12 represents the results of the optimization procedure using fused silica plates with thicknesses up to 5 mm. The maximum shift of the proton spectra is found with a thickness of 3 mm and corresponds to the shortest pulse duration available within our set–up inside the ion spectrometer. Moreover, one can infer from Fig. 12 that the total number of detected protons presents a minimum at the shortest pulse duration for a fused silica thickness of 3 mm. Indeed the shortest pulse duration is associated to a

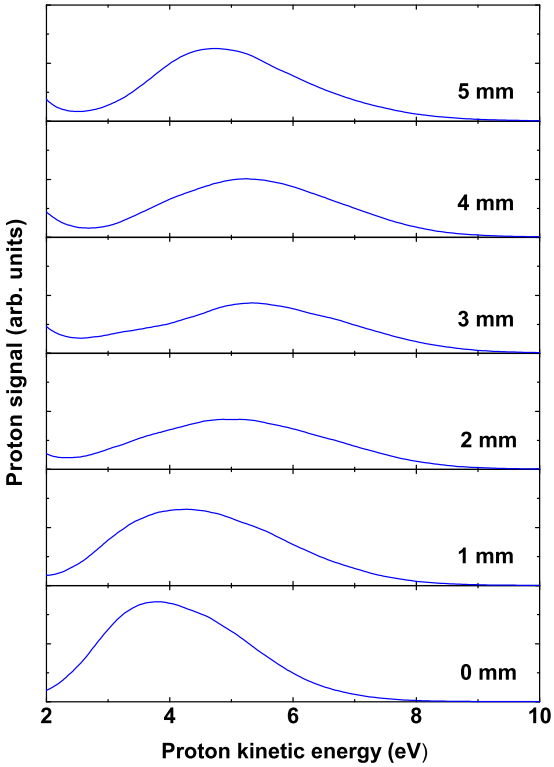

FIG. 12: (Color online) Optimization of the ultrashort pulse duration. Proton spectra from H_2 recorded at 2×10^{15} Wcm^{-2} with different thicknesses of fused silica from 0 to 5 mm inserted in the beam path before the ion spectrometer.

reduced internuclear range and hence to a higher energy gap in order to reach the double ionization $H^+ + H^+$ threshold. In addition, charge resonance enhanced ionization plays a minor role in comparison with larger internuclear distances produced with longer pulse durations. Finally, such a procedure was used with other molecules such as N_2 and O_2 and represents a straightforward method for pulse duration optimization [25].

B. Carrier–envelope phase dependence

The carrier–envelope phase dependence of strong field effects was first investigated in high–order harmonic generation and above–threshold ionization [35, 36]. Concerning molecular dissociation, Roudnev *et al.* have theoretically shown that it is possible to control the H_2^+ and HD^+ dissociation with the carrier–envelope phase [37]. More recently a first exper-

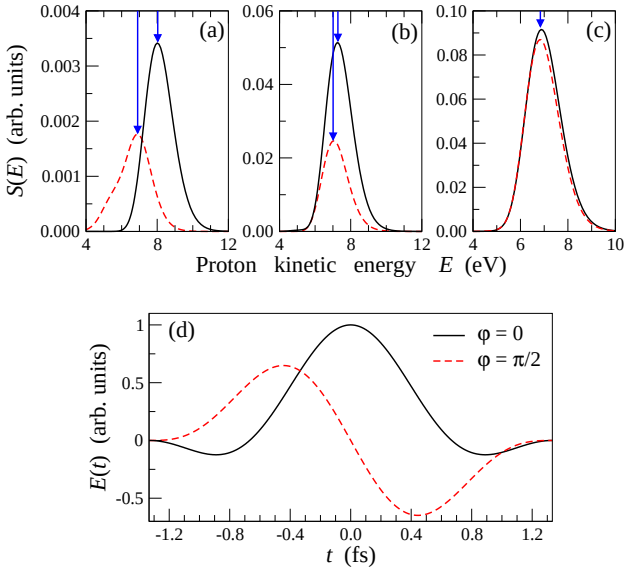

FIG. 13: (Color online) Calculated proton spectra from H_2 at 8×10^{14} Wcm^{-2} as a function of the carrier–envelope phase φ and the pulse duration. Full curves: $\varphi = 0$. Dashed curves: $\varphi = \pi/2$. The left (a), middle (b), and right (c) top panels correspond to different pulse durations of respectively 1 fs, 2 fs, and 4 fs. The vertical arrows mark the positions of the different peaks. The corresponding electric field is represented in the lower panel (d) as a function of time for a pulse duration of 1 fs.

imental evidence was given in the dissociative ionization of D_2 [13]. The carrier–envelope phase dependence of the intramolecular electronic motion leads to the localization of the electron on one or the other nucleus. Therefore, the resulting dissociation channels $D^+ + D$ and $D + D^+$, where the left or right position of the deuteron D^+ indicates its initial emission direction, can now be separated as a function of the carrier–envelope phase. Finally, Tong and Lin investigated the carrier-envelope phase dependence of nonsequential double ionization of H_2 by few–cycle laser pulses [38]. They found that the strong dependence of the double ionization yields is due to the return energy of the rescattering electron.

Here we address the question of the carrier-envelope dependence of the proton spectra from double ionization at laser intensities where double ionization is mainly sequential. In the nonsequential regime, Tong and Lin have shown that the proton spectra lie within the same proton energy range [38]. Moreover at laser intensities above 1.5×10^{14} Wcm^{-2} and a pulse duration of 5 fs, proton spectra from nonsequential double ionization are found to be independent on the initial phase. We theoretically confirm this tendency at higher

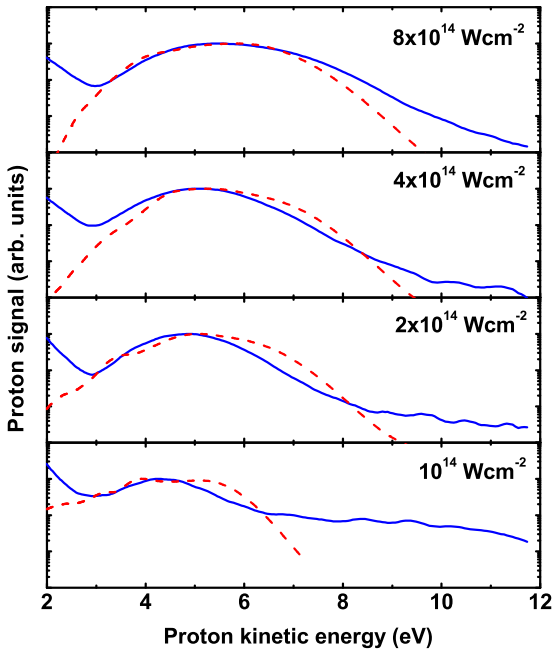

FIG. 14: (Color online) Proton spectra from H_2 at different laser intensities 8×10^{14}, 4×10^{14}, 2×10^{14}, and 10^{14} Wcm^{-2} from top to bottom. Full curves: Experimental. Dashed curves: Theoretical.

laser intensities in the sequential regime. Figure 13 represents proton spectra calculated at 8×10^{14} Wcm^{-2} for two values of the carrier-envelope phase $\varphi = 0$ and $\varphi = \pi/2$ rad. In addition, calculations were performed for three values of the laser pulse duration (a) 1 fs, (b) 2 fs, and (c) 4 fs. A significant shift of 1.2 eV is only observed for the 1–fs pulse whereas no energy shift is visible for a pulse duration of 4 fs. In addition a smaller production of H^+ ions is calculated with $\varphi = \pi/2$ as compared with $\varphi = 0$ for 1–fs and 2–fs pulses. One can also notice in Fig. 13(d) which represents the time dependence of the associated electric fields in the case of the 1–fs pulse, that a higher peak intensity is achieved with $\varphi = 0$. In consequence, the sequential ionization of the H_2^+ ion is more delayed at $\varphi = \pi/2$ than at $\varphi = 0$, thus resulting in a higher proton energy when $\varphi = 0$. However as the number of cycles increases within the pulse duration, this effect disappears and the proton energy range is no more dependent on the carrier–envelope phase.

C. Laser intensity dependence

Double ionization of hydrogen by infrared laser light is a highly nonlinear process. The intensity dependence therefore follows a complicated behaviour which has to be studied both from combined experimental and theoretical works. Figure 14 presents four experimental and theoretical proton spectra from 10^{14} to 8×10^{14} Wcm^{-2}. The spectra are shifted towards higher energies as the intensity is increased. The experimental spectra are maximum at 4.2 eV, 4.9 eV, 5.0 eV, and 5.5 eV at respectively 10^{14}, 2×10^{14}, 4×10^{14}, and 8×10^{14} Wcm^{-2}. This effect was also observed in multiple ionization of nitrogen and oxygen with pulse durations of 40 fs and 10 fs and comes from sequential electron emission [25, 39]. The time delay between the first ionization and the second ionization, leading respectively to H_2^+ and to $H^+ + H^+$, is reduced because the necessary instantaneous intensity for the second ionization comes sooner when the laser intensity is increased.

The experimental spectra are reasonably well reproduced by the model predictions with some differences mainly in the high energy sides of the spectra. In spite of these discrepancies, the model predicts the correct energy range of the expected proton spectra at 10 fs for different laser intensities. It therefore constitutes a worthy predictive tool for the use of ultrashort pulses when one considers the very complicated dynamics of the hydrogen molecular response. Several effects might explain the observed differences in addition to the laser and ion measurements uncertainties. The calculation is performed for one laser intensity and thus does not take into account the intensity distribution within the focal volume. This might explain the discrepancies in the high–energy wings of the spectra where nonsequential double ionization does play a noticeable role at low laser intensity [20]. Indeed for a given peak laser intensity, low intensities are distributed over a much larger volume than high intensities and may noticeably contribute to the observed discrepancies in Fig. 14.

V. SUMMARY AND CONCLUDING REMARKS

We have presented a detailed experimental and theoretical analysis of H_2 sequential double ionization using ultrafast laser pulses in the 10^{14}–10^{15} Wcm^{-2} intensity range. We have shown that the resulting proton spectra are very sensitive to the temporal, phase, and intensity characteristics of the pulse. More precisely, higher energy protons are emitted

when the pulse duration decreases and when the peak intensity increases. On the other hand, the effect of the carrier–envelope phase offset is only significant for pulse durations shorter than 4 fs.

The main characteristics of the measured proton spectra from double ionization of H_2 are well reproduced by a full quantum calculation based on the time–dependent Schrödinger equation. The R–dependent soft–Coulomb parameters introduced in this study make the model relatively simple and manageable using tractable computing facilities. These parameters are fitted using *ab initio* calculations of the ground electronic states of H_2 and H_2^+ as a function of the internuclear distance R. We are confident that the good agreement between experiment and theory at 10 fs allows to give valuable predictions for shorter laser pulses and in particular about the ultrafast dynamics of the H_2^+ ion as a function of the pulse duration, carrier–envelope phase offset and peak intensity.

The degree of control of few–cycle laser pulses becomes more and more sophisticated [13]. In this respect, the H_2 response to the associated high laser field might become a complementary diagnostic to ultrashort laser pulses in addition to the existing FROG and SPIDER techniques. In particular the relative simplicity of the proton detection associated to a reliable model might be of some interest in ultrafast laser physics.

Acknowledgments

We acknowledge high performance computing facilities of the IDRIS-CNRS center (Project No. 06-1459) and financial support from ACI Photonique Physique Attoseconde, from CEA via LRC-DSM Grant No. 05-33, and from ANR Image Femto (Project No. BLAN07-2_201076). Laboratoire de Photophysique Moléculaire is associated to Université Paris-Sud.

---

[1] M. Nisoli, S. De Silvestri, and O. Svelto, Appl. Phys. Lett. **68**, 2793 (1996).

[2] S. Sartania, Z. Cheng, M. Lenzner, G. Tempea, C. Spielmann, F. Krausz, and K. Ferencz, Optics Lett. **22**, 1562 (1997).

[3] P. M. Paul, E. S. Toma, P. Breger, G. Mullot, F. Augé, P. Balcou, H. G. Muller, and P. Agostini, Science **292**, 1689 (2001).

[4] Y. Mairesse, A. de Bohan, L. J. Frasinski, H. Merdji, L. C. Dinu, P. Monchicourt, P. Breger, M. Kovačev, R. Taïeb, B. Carré, et al., Science **302**, 1540 (2003).

[5] D. Kane and R. Trebino, IEEE J. Quantum Electron. **29**, 571 (1993).

[6] C. Iaconis and I. Walmsley, Optics Lett. **23**, 79 (1998).

[7] Y. Mairesse and F. Quéré, Phys. Rev. A **71**, 011401 (2005).

[8] G. Sansone, E. Benedetti, F. Calegari, C. Vozzi, L. Avaldi, R. Flammini, L. Poletto, P. Villoresi, C. Altucci, R. Velotta, et al., Science **314**, 443 (2006).

[9] A. Giusti-Suzor, F. H. Mies, L. F. Di Mauro, E. Charron, and B. Yang, J. Phys. B: At. Mol. Opt. Phys. **28**, 309 (1995).

[10] J. H. Posthumus, ed., *Molecules and clusters in intense laser fields* (Cambridge University Press, 2001).

[11] J. H. Posthumus, Rep. Prog. Phys. **67**, 623 (2004).

[12] H. Niikura, F. Légaré, R. Hasbani, M. Yu Ivanov, D. M. Villeneuve, and P. B. Corkum, Nature **421**, 826 (2003).

[13] M. Kling, C. Siedschlag, A. Verhoef, J. Kahn, M. Schultze, T. Uphues, Y. Ni, M. Uiberacker, M. Drescher, F. Krausz, et al., Science **312**, 246 (2006).

[14] S. Saugout and C. Cornaggia, Phys. Rev. A **73**, 041406 (2006).

[15] T. Zuo and A. D. Bandrauk, Phys. Rev. A **52**, R2511 (1995).

[16] F. Légaré, I. Litvinyuk, P. Dooley, F. Quéré, A. Bandrauk, D. Villeneuve, and P. Corkum, Phys. Rev. Lett. **91**, 093002 (2003).

[17] X. Tong, Z. Zhao, and C. Lin, Phys. Rev. Lett. **91**, 233203 (2003).

[18] X. Tong and C. Lin, Phys. Rev. A **70**, 023406 (2004).

[19] A. Alnaser, X. Tong, T. Osipov, S. Voss, C. Maharjan, P. Ranitovic, B. Ulrich, B. Shan, Z. Chang, C. Lin, et al., Phys. Rev. Lett. **93**, 183202 (2004).

[20] C. Beylerian, S. Saugout, and C. Cornaggia, J. Phys. B: At. Mol. Opt. Phys. **39**, L105 (2006).

[21] A. Rudenko, B. Feuerstein, K. Zrost, V. de Jesus, T. Ergler, C. Dimopoulou, C. Schröter, R. Moshammer, and J. Ullrich, J. Phys. B: At. Mol. Opt. Phys. **38**, 487 (2005).

[22] S. Saugout, C. Cornaggia, A. Suzor-Weiner, and E. Charron, Phys. Rev. Lett. **98**, 253003 (2007).

[23] D. Strickland and G. Mourou, Opt. Comm. **56**, 219 (1985).

[24] W. C. Wiley and I. McLaren, Rev. Sci. Instrum. **26**, 1150 (1955).

[25] E. Baldit, S. Saugout, and C. Cornaggia, Phys. Rev. A **71**, 021403 (2005).

[26] L. J. Frasinski, K. Codling, and P. A. Hatherly, Science **246**, 973 (1989).

[27] P. Hering and C. Cornaggia, Phys. Rev. A **59**, 2836 (1999).

[28] K. Harumiya, H. Kono, Y. Fujimura, I. Kawata, and A. D. Bandrauk, Phys. Rev. A **66**, 043403 (2002).

[29] S. Baier, C. Ruiz, L. Plaja, and A. Becker, Phys. Rev. A **74**, 033405 (2006).

[30] J. Peek, J. Chem. Phys. **43**, 3004 (1965).

[31] W. Kolos and L. Wolniewicz, J. Chem. Phys. **43**, 2429 (1965).

[32] M. J. Feit, J. A. Fleck, and A. Steiger, J. Comput. Phys. **47**, 412 (1982).

[33] R. Kosloff and H. Tal-ezer, Chem. Phys. Lett. **127**, 223 (1986).

[34] A. I. Pegarkov, E. Charron, and A. Suzor-Weiner, J. Phys. B: At. Mol. Opt. Phys. **32**, L363 (1999).

[35] A. Baltuška, T. Udem, M. Uiberacker, M. Hentschel, E. Goulielmakis, C. Gohle, R. Holzwarth, V. Yakovlev, A. Scrinzi, T. Hänsch, et al., Nature **421**, 611 (2003).

[36] G. Paulus, F. Lindner, H. Walther, A. Baltuška, E. Goulielmakis, M. Lezius, and F. Krausz, Phys. Rev. Lett. **91**, 253004 (2003).

[37] V. Roudnev, B. Esry, and I. Ben-Itzak, Phys. Rev. Lett. **93**, 163601 (2004).

[38] X. Tong and C. Lin, J. Phys. B: At. Mol. Opt. Phys. **40**, 641 (2007).

[39] L. Quaglia, O. Chiappa, G. Granucci, V. Brenner, P. Millié, and C. Cornaggia, J. Phys. B: At. Mol. Opt. Phys. **35**, L145 (2002).